Faculty of Engineering and Information Sciences - Papers: Part A

2015

Crystal plasticity finite element method modelling of indentation size effect

Mao Liu
University of Wollongong, ml818@uowmail.edu.au

Cheng Lu
University of Wollongong, chenglu@uow.edu.au

A Kiet Tieu
University of Wollongong, ktieu@uow.edu.au

Crystal plasticity finite element method modelling of indentation size effect

Abstract

A crystal plasticity finite element method (CPFEM) model has been developed to investigate the indentation size effect (ISE) of aluminium single crystal during nano-indentation. The simulated results have been validated by comparison with experimental observations. The load-hardness curves from simulation are consistent with the experimental results. The mathematic relationship between load and indentation depth has been built to investigate indentation size effect. In addition, the Mises stress, critical resolved shear stress, stress and shear strain rates for a selected element and the lattice curvature have been studied to explain indentation size effect.

Crystal plasticity Finite Element Method modelling of indentation size effect

Mao Liu, Cheng Lu[1], Anh Kiet Tieu

School of Mechanical, Materials and Mechatronic Engineering, University of Wollongong, Wollongong, NSW 2522, Australia

Abstract

A crystal plasticity finite element method (CPFEM) model has been developed to investigate the indentation size effect (ISE) of aluminium single crystal during nano-indentation. The simulated results have been validated by comparison with experimental observations. The load-hardness curves from simulation are consistent with the experimental results. The mathematic relationship between load and indentation depth has been built to investigate indentation size effect. In addition, the Mises stress, critical resolved shear stress, stress and shear strain rates for a selected element and the lattice curvature have been studied to explain indentation size effect.

Keywords: Crystal plasticity finite element method; Nano-indentation; Indentation size effect (ISE); Lattice curvature; Aluminium single crystal

1. Introduction

Since the 1950s (Swadener et al., 2002), a great number of researchers have found that the microscopic mechanical properties of materials are significantly different to those of bulk materials at the macro-scale. For example, the measured indentation hardness of metallic materials increases sharply as the penetration depth decreases at the nano-scale. This phenomenon was named "indentation size effect (ISE)". The earlier study of ISE was done by Mott (Swadener et al., 2002) and then numerous other researches followed his study. For example, Gane and Cox (Gane and Cox, 1970) reported that hardness could be increased by a factor of three by decreasing the contact diameter from 10^4 to 10^2 nm for an Au single crystal. Stelmashenko et al. (Stelmashenko et al., 1993) and Ma and Clark (Ma and Clark, 1995) found that hardness increase greatly with the depths less than 1 μm. Fleck and Hutchinson (Fleck and Hutchinson, 1993, 1997) believed classical plasticity theory cannot predict ISE as its constitutive model did not include intrinsic (internal) length scale. Therefore, they developed a strain gradient plasticity model which included material length scale which is

---

[1] Corresponding author: Lu C.: chenglu@uow.edu.au
Tel: +61 2 42214639

thought of as an internal material length related to storage of geometrically necessary dislocations. They also found this internal material length is approximately 4 microns for copper. Subsequently, by considering the geometrically necessary dislocations (GND), Nix and Gao (Nix and Gao, 1998) developed a mechanism-based model which agrees well with experiments. This model then was further modified by Gao et al. (Gao et al., 1999a; Gao et al., 1999b) and Huang et al. (Huang et al., 2000). It was believed, the GNDs would accumulate underneath an indenter during the deformation process. Meanwhile, these dislocations could provide work hardening to the material and therefore increase the indentation hardness. Nix and Gao (Nix and Gao, 1998) strain gradient model was believed to be the best way to simulate and explain the ISE afterwards. However, it soon had been found that the main assumptions for that model are in conflict with the experimental observations. Kiener (Kiener et al., 2009) investigated Nix-Gao model (Nix and Gao, 1998) with the cross-sectional EBSD method and proposed that Nix-Gao model (Nix and Gao, 1998) physical basis was still under debate, and its validity cannot be addressed alone with load versus displacement characteristics.There were two assumptions with respect to the Nix-Gao model (Nix and Gao, 1998), hemispherical plastic zone and self-similarity of the evolving deformation structure. However, according to the EBSD observation, the ture plastic deformed zone was found to deviate from the assumption of a half-sphere. Other reports indicated that there were differently shaped deformation areas, depending on the indenter geometry (Kiener et al., 2006; Rester et al., 2007; Zaafarani et al., 2006). Regarding the self-similarity, based on the Nix-Gao model (Nix and Gao, 1998), the strain gradient induced by the indenter should be determined solely by the indenter geometry. Therefore, it should be constant for self-similar indenter shapes, which means the observed misorientations should depend only on the indenter angle and not on the indent size. However, the obsevations for Vickers indents in copper and tungsten displayed that the maximum misorientation was along the indent flanks for different sizes. According to the experimental results, they concluded that the explaination size-dependent material strengthening effects by using average density measure for GNDs was not sufficient to understand the indentation size effect.

Meyer's law is another widely used method to describe ISE. For the indenters which have ideal geometry, the relationship between the test load and the resultant indentation diagonal length curve could be obtained from (Ebisu and Horibe, 2010)

$$P = C \cdot d^n \qquad (1)$$

where P is the load, d is the diagonal length of impression, C is the material/indenter constant and n is the Meyer index due to the curvature of the curve. Since d is proportional to the contact depth h_c which in turn is proportional to the indentation depth h, Eq. (1) could be expressed as follows:

$$P = C' \cdot h^n \qquad\qquad (2)$$

where C' is constant and h is the indentation depth.

Fischer-Cripps (Fischer-Cripps, 2006) mentioned that if the plastic zone was fully developed (beyond elastic-plastic transition point), the load-displacement(P-h) curve of the loading section could be related to the square of the displacement ($P = C'h^2$). As for the loading stage of the P-h curve in the elastic-plastic field. Sakai (Sakai, 1993) stated that the load is proportional to the square of the indentation depth. According to Eq. (1), if n=2, the materials shows no ISE. But if n<2, the materials shows ISE and this case was confirmed by different materials (Gong et al., 1999; Ren et al., 2003).

However, Peng et al. (Peng et al., 2004) pointed out the correlation between n and C seemed to be of little significance for understanding the ISE, as their previous study has showed that the best-fit value of the Meyer's law coefficient C depended on the unit system used for recording the experimental data and completely different trends of n versus C may be observed in different unit systems (Gong et al., 2000) as shown in Fig. 1
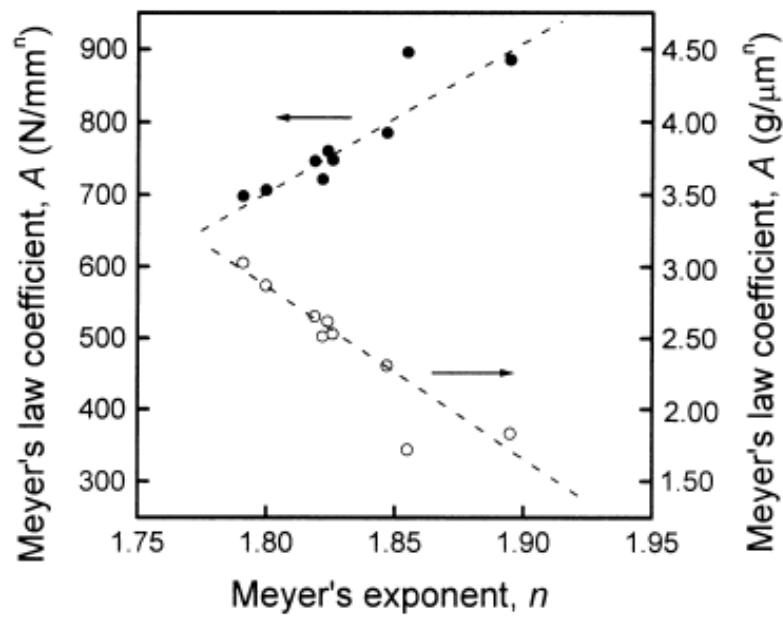
Fig. 1. Variation of Meyer's law coefficient C with Meyer's exponent n. Note that completely different trends are observed when different unit systems were used for recording the experimental data. (Gong et al., 2000)

The first unit system used is P in Newton (N) and d in milli-meter (mm) and the second is P in gram (g) and d in micrometer (mm). As can be seen from Fig. 1, completely different trends of n versus A were observed in different unit systems. Similar conclusions were reported by Li and Bradt (Li and Bradt, 1993) when they analyzed the experimental data on single crystals. Thus, they concluded that a particular care should be taken when analyzing the microstructural effects on the measured hardness based on Meyer's power law.

It should be noted that only n plays an improtant role in determining ISE in Meyer's law and it is not necessary to consider the variation of Meyer's law coefficient C. Although numerous researchers used Meyer's law to analyse ISE, all of them just fit the whole P-h curve. In fact, the P-h curve can be fitted separately from the ISE-boundary which is shown as in Fig. 2. In the left side of ISE-boundary a n-value smaller than 2 can be obtained, while a n-value of about 2 can be achieved in the right side.
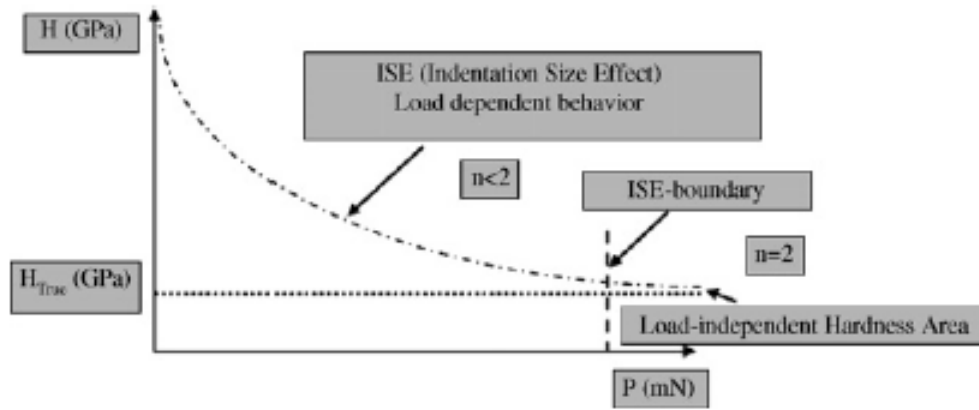
Fig. 0. Schematic plot of the ISE behaviour. (Kolemen, 2006)

Other potential influence factors, such as inadequate measurement capabilities of extremetly small indents (Samuels, 1986), presence of oxides or chemical contamination on the surface (Sargent, 1986), indenter-specimen friction (Li et al., 1993), increased dominance of edge effects with shallow indents (Ma and Clark, 1995) and tip radius(McElhaney et al., 1998) have been eventually proven to be ineffective in determing the ISE.

In this chapter, the CPFEM model has been developed to predict the ISE. The mathematic relationship between load and indentation depth has been built to investigate indentation size effect. Meanwhile, the Mises stress, critical resolved shear stress, stress and shear strain rates for a selected element and the lattice curvature have been studied to explain indentation size effect.

2. **Three-dimensional CPFEM simulation model**

The crystal plasticity theory is based on the assumption that plastic deformation is the cumulative effect of crystalline slips in all activated slip systems. The details of the crystal plasticity theory can be found in Ref (Si et al., 2008). The crystal plasticity constitutive model used in the present study follows the approach described by Asaro (Asaro, 1983). This was incorporated into the implicit finite element code ABAQUS/Standard through a user-defined material subroutine (UMAT). The UMAT subroutine provides the material Jacobian matrix

for the constitutive model, and updates the stresses and the solution-dependent state variables as the solution proceeds. In the present study, we adopted the UMAT framework initially developed by Huang (Huang, 1991) and also used Bassani and Wu's (Bassani and Wu, 1991) formulation as the hardening model which has been described in Ref.(Lu et al., 2011). The formulations of the rate-dependent hardening model used in the present study can be expressed as

$$\dot{\gamma}^{(\alpha)} = \dot{\gamma}_0^{(\alpha)} \text{sgn}\left(\tau^{(\alpha)}\right) \left| \tau^{(\alpha)} \middle/ \tau_c^{(\alpha)} \right|^m \tag{3}$$

and

$$\text{sgn(x)} = \begin{cases} -1, & x < 1 \\ 1, & x \geq 1 \end{cases} \tag{4}$$

where $\dot{\gamma}_0^{(\alpha)}$ is the reference (initial) value of the shear strain rate, which is a constant for all slip systems. m is the strain rate sensitive exponent. Both $\dot{\gamma}_0^{(\alpha)}$ and m are the material parameters. $\tau_c^{(\alpha)}$ is the critical resolved shear stress of the slip system α, which represents the strength of the material.

The rate of change of the critical resolved shear stress is expressed by (Hill, 1966):

$$\dot{\tau}_c^{(\alpha)} = \sum_{\beta=1}^{N} f_{\alpha\beta} h_{\alpha\beta} \, \dot{\gamma}^{(\beta)} \tag{5}$$

$$h_{\alpha\alpha} = \left[(h_0 - h_s)sech^2\left((h_0 - h_s)\gamma^{(\alpha)} \middle/ \tau_1 - \tau_0 \right) + h_s \right]\left[1 + \sum_{\substack{\beta=1 \\ \beta \neq \alpha}}^{N} f_{\alpha\beta}\tanh(\gamma^{(\beta)} \middle/ \gamma_0) \right],$$

$$for \ \alpha = \beta \tag{6a}$$

$$h_{\alpha\beta} = qh_{\alpha\alpha}, \quad for \ \alpha \neq \beta \tag{6b}$$

where $h_{\alpha\beta}$ is the hardening modulus including the self-hardening of each system ($\alpha=\beta$) and latent hardening ($\alpha\neq\beta$); q is the latent hardening parameter; γ_0 is the reference value of slip; γ is the shear strain; τ_0 is the initial critical resolved shear stress; τ_1 is the breakthrough stress where large plastic flow initiates; h_0 is the hardening modulus just after initial yield; h_s is the hardening modulus during easy glide and $f_{\alpha\beta}$ is the magnitude of the strength of a particular slip interaction between two slip systems α and β. The factor $f_{\alpha\beta}$ depends on the geometric relation between two slip systems. There are five constants for $f_{\alpha\beta}$: α_1 (no junction), α_2 (Hirth lock), α_3 (coplanar junction), α_4 (glissile junction) and α_5 (sessile junction).

A three dimensional model has been developed to simulate the deformation behaviour of nano-indentation, as shown in Fig. 3. The indenter used in this study is a conical indenter with a 70.3° semi-angle which has the same area-to-depth ratio as the Berkovich tip. The diameter of the tip is 400nm. The simulated specimen consisted of 17040 eight-node brick elements and 18352 nodes with reduced integration (element id: C3D8R) to ensure that the mesh was fine enough, especially the area that makes contact with the indenter. The total number of nodes and elements are about 7 times more than those used in most published papers (Liu et al., 2008; Liu et al., 2005). The depth of indentation in this study is also larger (2000 nm) than that in the published literatures (300nm) (Liu et al., 2008; Liu et al., 2005). The X, Y, and Z coordinates represent the rolling direction (RD), the transverse direction (TD), and the normal direction (ND), respectively. The simulations were carried on the Cube oriented surface of single crystal aluminium, which suggests the orientation directions along the X, Y and Z axes are [0 0 1], [0 1 0] and [0 0 1], respectively. The dimensions of the specimen in the FEM model are 40 μm × 40 μm × 20 μm. The height of the simulated specimen is much larger than the maximum depth of indentation of 2 μm in order to avoid the influence from the boundary condition (Fischer-Cripps, 2009).

Franciosi et al. (Franciosi et al., 1980) and Lu et al. (Lu et al., 2011) reported that the factor $f_{\alpha\beta}$ can be chosen as $a_1 = a_2 = a_3 = 1.75$, $a_4 = 2$ and $a_5 = 2.25$ for single crystal aluminium. Three elastic moduli used were C_{11} = 112 GPa, C_{12} = 66 GPa and C_{44} = 28 GPa. Table 1 shows the other material parameters used in the hardening model (Eqs. (3)-(6)). These parameters have been validated in the CPFEM simulations of nano-indentation, rolling, tensile test and equal-channel angular pressing (Huynh et al., 2008; Liu et al., 2014; Lu et al., 2011; Si et al., 2008). There is only one set of slip systems for FCC (face-centered cubic)

metals, {111}<110>, which includes 12 different slip systems shown in Table 2. In the deformed single crystal aluminum, slips occur on the {111} planes and in the <110> directions.

Table 1 Parameters used in the work-hardening model.

m	$\dot{\gamma}_0$ (1/s)	h_0 (MPa)	h_s (MPa)	τ_1 (MPa)	τ_0 (MPa)	γ_0	q
300	0.0001	100	0.01	6.3	6	0.001	1

Table 2 Notation of the slip systems for the FCC materials considered in this study.

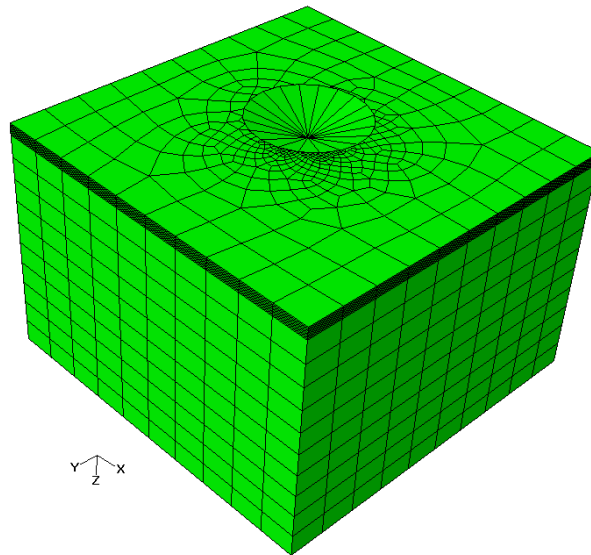| System	a1	a2	a3	b1	b2	b3	c1	c2	c3	d1	d2	d3
Plane	(111)			$(11\bar{1})$			$(\bar{1}11)$			$(1\bar{1}1)$		
Direction	$[0\bar{1}1]$	$[10\bar{1}]$	$[\bar{1}10]$	[011]	[101]	[110]	$[0\bar{1}1]$	[101]	[110]	[011]	$[10\bar{1}]$	[110]

Fig. 3. 3D nano-indentation model setup

All the nodes on the bottom surface and four surrounding surfaces of the specimen were constrained along three normal directions. A fixed time step increment 0.01 s is chosen and a total time step increments of 24,062 in the simulation are used, including contact, loading, and unloading.

The indentation hardness can be calculated according the following equations.

$$H = \frac{P}{A_c} \tag{7}$$

$$A_c = 3\sqrt{3}{h_c}^2 tan^2 65.3 = 24.56{h_c}^2 \tag{8}$$

$$h_c = h_{max} - k\frac{P_{max}}{S}, k = 0.75, S = \left(\frac{dP}{dh}\right)_{h=h_{max}} \tag{9}$$

where H is the indentation hardness, A_c is the contact area between indenter and deformed surface, h_c is the contact depth.

The simulated results have been compared with the experimental data obtained by Voyiadjis and Peter (Voyiadjis and Peters, 2010) in 2009 who conducted the nano-indentation tests on the polished surface of a 99.9999% purity poly-crystal aluminium sample. As indents normally locate in a single grain, it can also been treated as a single crystal. The conical indenter with a 70.3° seme apex angle has been used in the simulations. Two simulations have been performed. The maximum indentation depths in two simulations are 2000 nm and 110nm, respectively. The simulated result of 2000nm depths is shown as in Fig. 4. The figure shows that both simulated and experimental results have the same tendency.
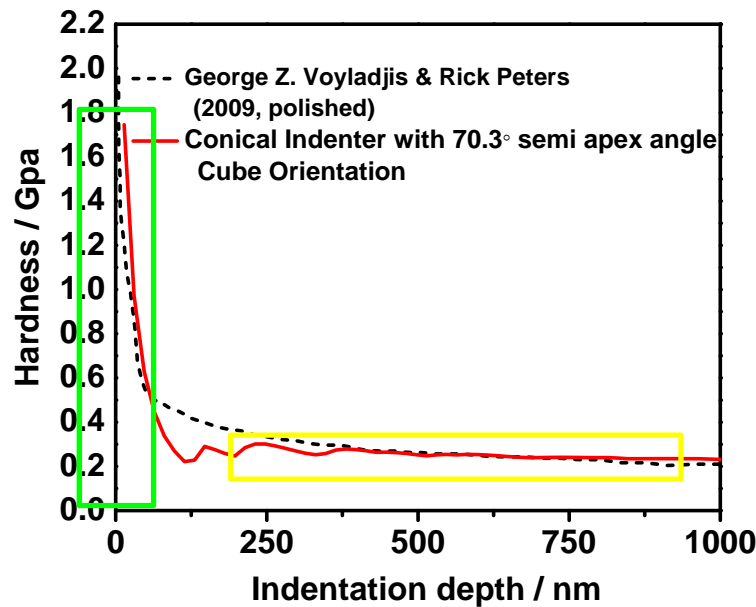

Fig. 4. Comparison of numerical (Conical indenter) and experimental indentation hardness-displacement curve.
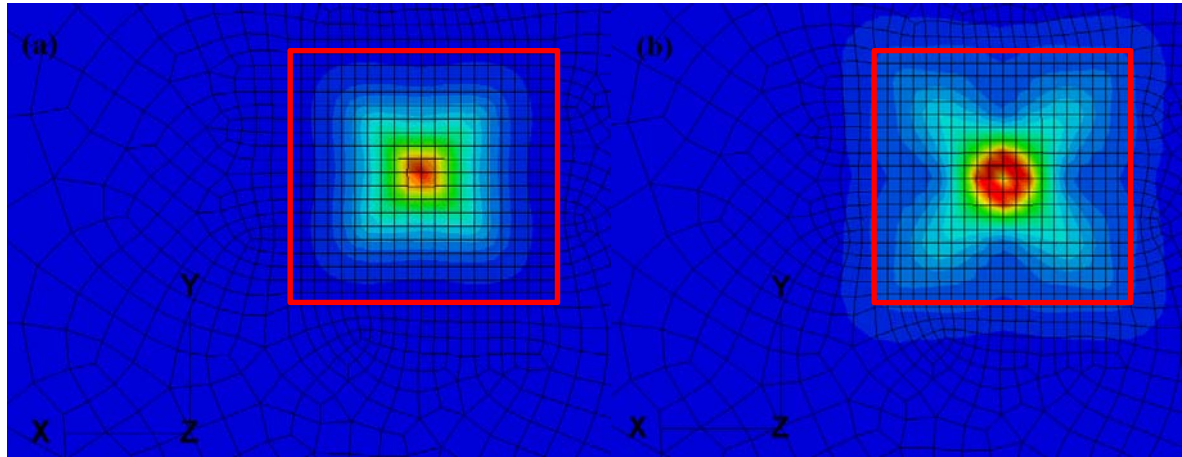
3. **Results and discussion**

Fig.5 The deformation of elements with the indentation depth of: (a)100nm; (b)200nm

Fig. 5 shows the deformation of elements at the beginning of the indentation. It is known that only finer mesh in the center of the sample is important for the accuracy of nano-indentation simulation, the coarser mesh in other regions is not sensitive to the simulation. From Fig.5, it is clear that most of elements in the center region have already been deformed even the indentation depth is shallow.
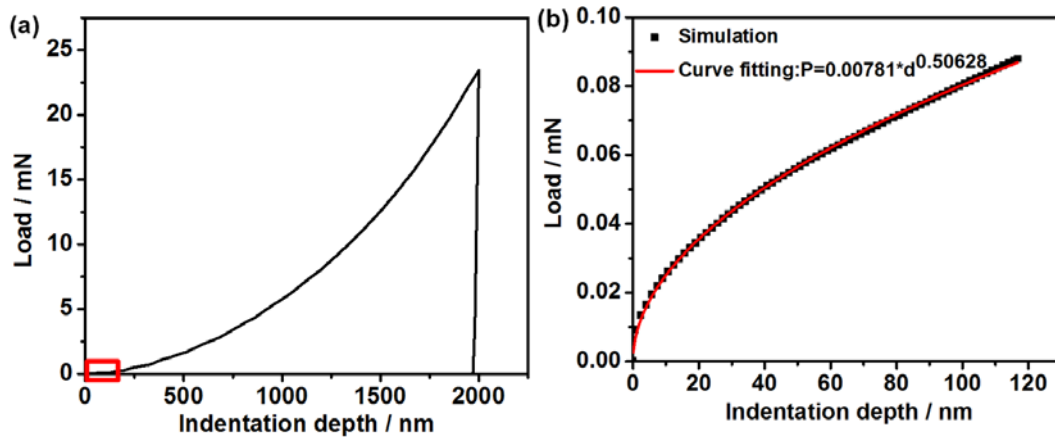

Fig. 6. Simulated load-displacement curve using conical indenter: (a) full loading/unloading curve for the maximum indentation depth (d) of 2000 nm; (b) the enlarged loading curve for the range of the indentation depth from 0 nm to 110 nm.
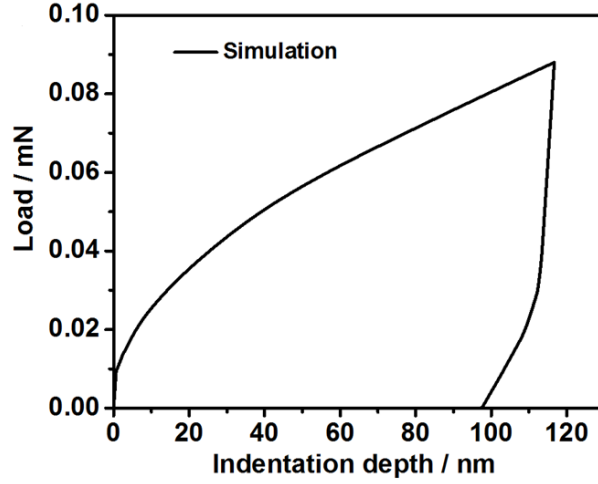
Fig. 7. Simulated load-displacement curve using conical indenter with full loading/unloading curve for the maximum indentation depth d of 110 nm.

Fig. 6 shows the simulated load-displacement curve using the conical indenter on the Cube initial oriented surface. Fig. 6(a) gives the full loading/unloading curve for the maximum indentation depth d of 2000 nm, while Fig. 6(b) shows the enlarged loading curve for a range of the indentation depths from 0 nm to 110 nm. It can be seen that for the lower indentation depth (d<110nm), the loading curve is convex, while it is concave for the higher indentation depth (d≥110nm).

In order to analyse the indentation size effect, the loading curve in the red rectangle marked in Fig. 6 is curve-fitted by a power relationship. The result can be expressed by

$$P = 0.00781 x d^{0.50628} \qquad (0 < d < 110nm) \qquad (10)$$

where P is the indentation load and d is the penetration depth. As the slop of unloading curve is very sharp (shown is Fig. 7), the contact depth h_c can be replaced by displacement d. Substituting Eq. (10) into Eq. (7), it is easy to obtain

$$H = \frac{P}{A_c} = \frac{3.2 x 10^{-4}}{d^{1.49372}} \qquad (11)$$

It can be known from Eq. (11) that when the penetration depth d increases from 0 to around 110 nm the indentation hardness H decreases significantly.

The loading part corresponding to the larger indentation depth (d≥110nm) can be regressed by the following expression:

$$P = 1.016 x 10^{-5} x d^{1.921} \qquad (12)$$

Likewise, the hardness can be expressed by

$$H = \frac{P}{A_c} = \frac{4.137x10^{-7}}{d^{0.079}} \tag{13}$$

As the exponent 0.079 is close to 0, the indentation hardness will nearly remain constant as the indentation depth changes.
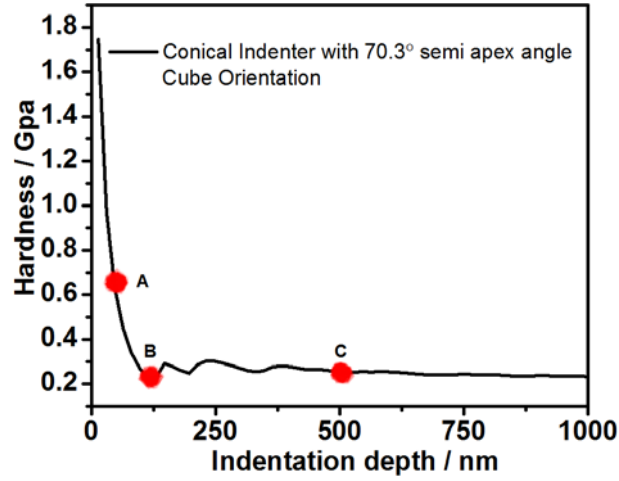

Fig. 8. Simulated indentation hardness-displacement curve with three characteristic points.

Fig. 8 shows the simulated indentation hardness-displacement curve with three characteristic stages (Stages A, B and C) during the indentation process. Stages A, B and C will be used to further understand ISE. The distribution maps of Mises stress, critical resolved shear stress and lattice curvature at three different stages will be analysed.
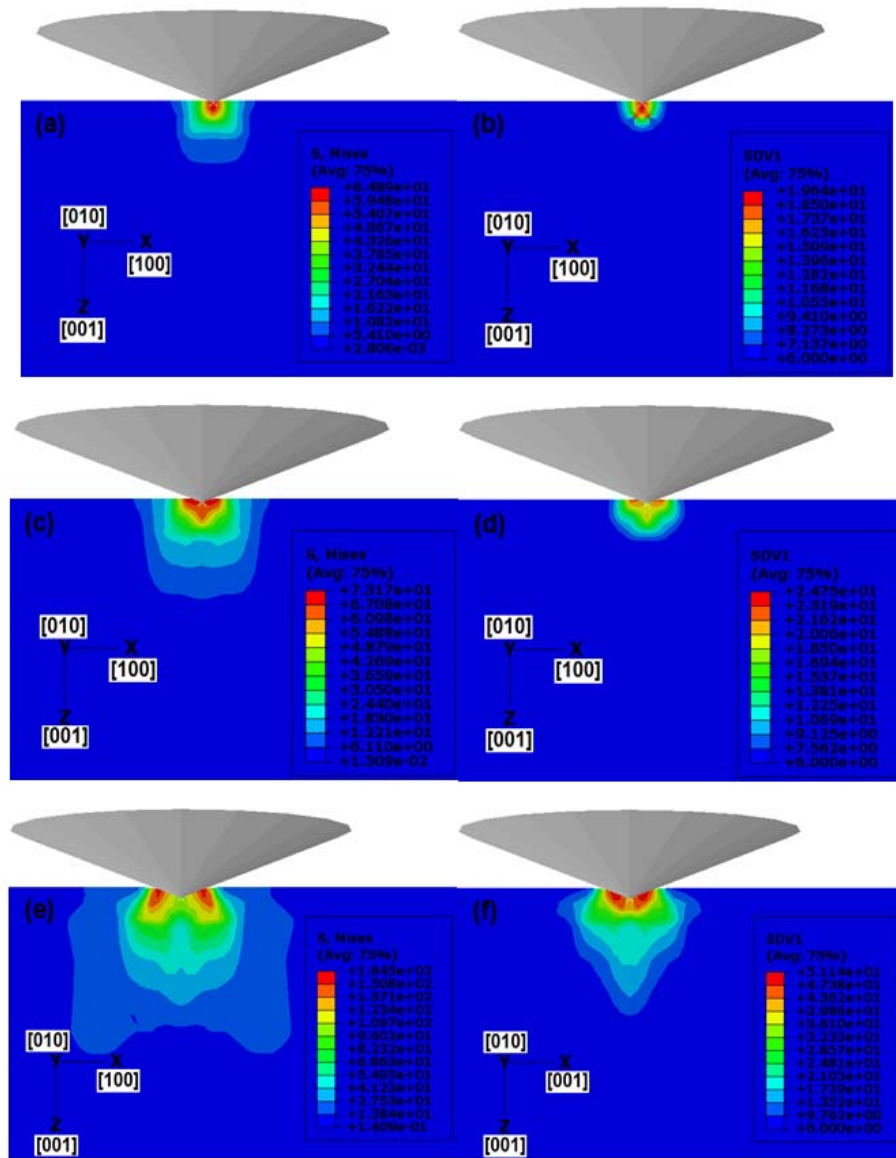
Fig. 9. The distribution of Mises stress and critical resolved shear stress (SDV1) at different stage during indentation: (a) stage A; (b) stage B; (c) stage C.

Fig. 9 shows the distribution map of Mises stress and critical resolved shear stress (SDV1) at different stages during indentation. It is clear both the maximum Mises stress and critical resolved shear stress are located right under the indenter at Stage A. However, both the maximum Mises stress and critical resolved shear stress start to split at Stage B. Finally, the maximum Mises stress and critical resolved shear stress move to the side of the indenter.
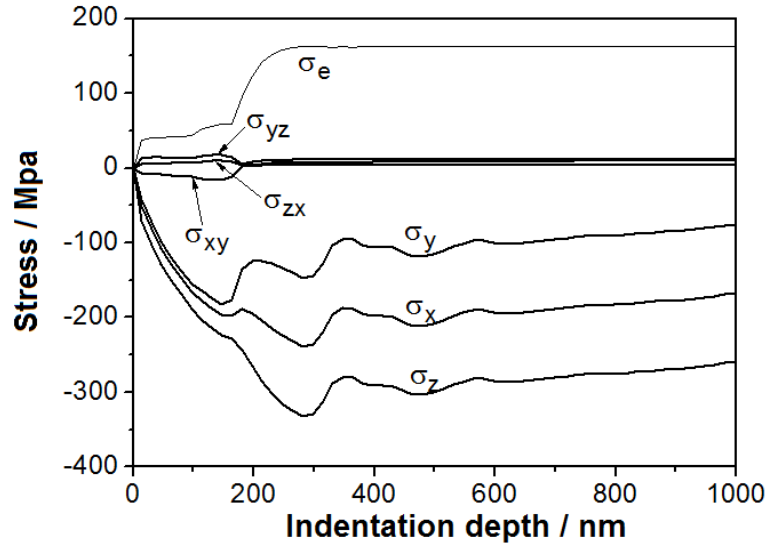
Fig. 10. Stress for a selected element under the indenter tip.

Fig. 10 shows the stress for a selected element under the indenter tip. It is clear the stresses increase quickly at the beginning of indentation and then remain constant. Fig. 11 shows shear strain rates of 12 slip systems for the same selected element below the indenter tip. Four slip systems (a2, a3, b1 and b3) were activated at the beginning of the indentation, and another two slip systems (c1, and c2) became active for indentation depth of 100-200 nm. According to the hardening model, $\dot{\gamma}^{(\alpha)} = \dot{\gamma}_0^{(\alpha)} \mathrm{sgn}(\tau^{(\alpha)}) \left| \frac{\tau^{(\alpha)}}{\tau_c^{(\alpha)}} \right|^m$, when the resolved shear stress on the primary slip system is much larger than the critical shear stress, the shear strain rate has a relatively larger value. This larger shear stress also results in larger resolved shear stress on other slip system, which finally activates another slip system at the same time. Once another slip system is activated, the higher shear stress occurs on the secondary slip system because of the result of very high initial hardening rate when these secondary systems are activated. Or in other words, the flow stress on the secondary slip system becomes higher than the one of the primary slip system because of the high hardening rate. The lager flow stress σ correlates with indentation hardness in the formation of $H = C\sigma$ which will help to explain why the hardness is so big at the beginning of the indentation.
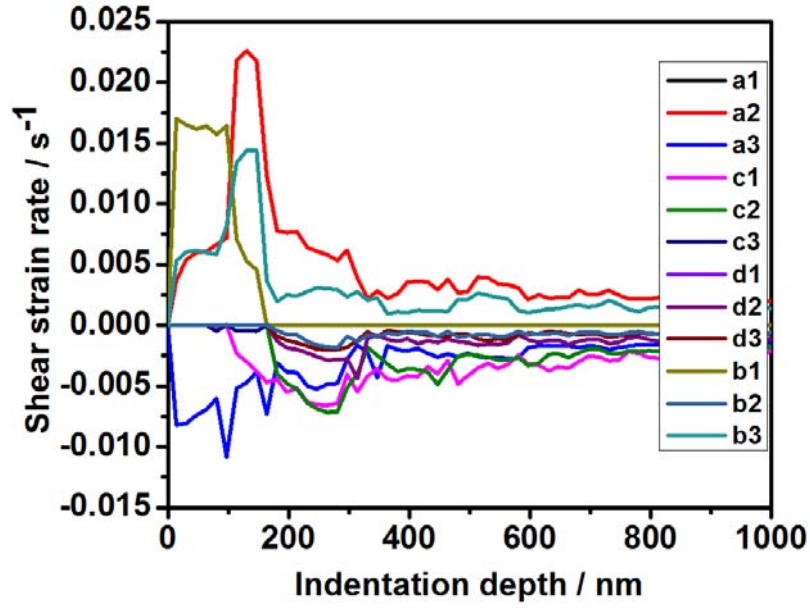
Fig. 11. Shear strain rates of 12 slip systems for a selected element below the indenter tip.

It is well known that GND density is meaningful for quantitatively characterizing strain gradient which is also determined by crystallographic orientation gradient. It is clear the crystallographic orientation gradient is the most important factor when investigating the strain gradient which is used to popularly explain indentation size effect. Arsenlis and Parks (Arsenlis and Parks, 1999) and Sun et al. (Sun et al., 2000) studied the crystallographic orientation dependence of GND before.

The lattice rotation angle with respect to $x(x_1)$, $y(x_2)$ and $z(x_3)$ coordinates is defined as ω_1, ω_2 and ω_3, respectively. The relationship between the global $x(x_1)$, $y(x_2)$ and $z(x_3)$ coordinates and the local $x'(x_1')$, $y'(x_2')$ and $z'(x_3')$ coordinates are shown in Fig. 12.
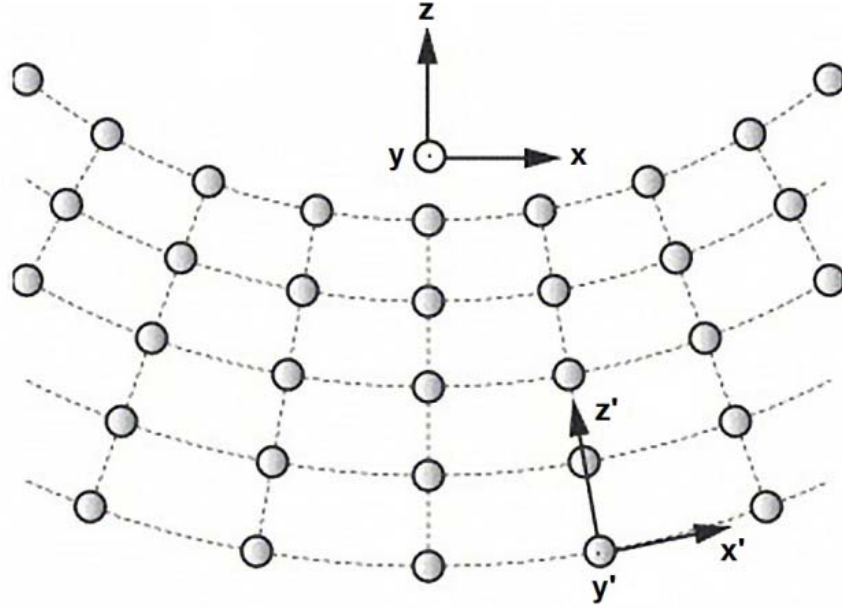
Fig. 12. Schematic drawing shows crystal lattice curvature, global and local coordinate systems. (Kysar et al., 2007)

The crystal lattice curvature tensor, k_{ij} , defined by Nye (Nye, 1953) is

$$k = \begin{pmatrix} k_{11} & k_{12} & k_{13} \\ k_{21} & k_{22} & k_{23} \\ k_{31} & k_{32} & k_{33} \end{pmatrix} \tag{14}$$

The component can be expressed by (Budiman et al., 2008; Budiman et al., 2006; Fleck et al., 1994)

$$k_{ij} = \frac{\partial \omega_i}{\partial x_j} \approx \frac{\Delta \omega}{\Delta x} \tag{15}$$

where, $\partial \omega / \partial x$ is the strain gradient, and Δx is the transition distance along x axis. $\Delta \omega$ represents the local lattice rotation with respect to the undeformed lattice , which is shown in Fig. 13 as follows
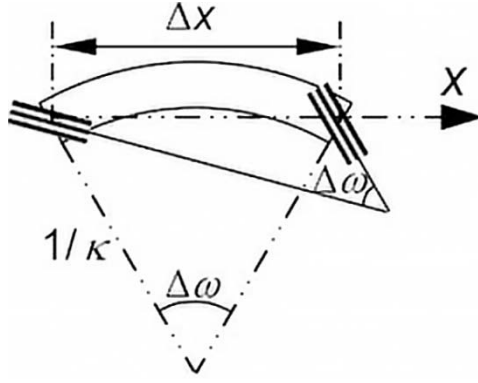
Fig. 13. The schematic of lattice curvature. (Feng et al., 2008)

Due to plane strain conditions with y-axis perpendicular to the (010) plane in our 3D indentation model, it is clear $\omega_1 = 0$, $\omega_3 = 0$, and $\omega_2 = \omega_y$. ω_y represents the in-plane rotation angle which can be calculated based on the method reported by Wert et al. (Wert et al., 1997). For the plane strain deformation state, only two of the nine components of k_{ij} are not equal to zero and they are

$$k_{21} = \frac{\partial \omega_2}{\partial x_1} = \frac{\partial \omega_2}{\partial x} \tag{16}$$

$$k_{23} = \frac{\partial \omega_2}{\partial x_3} = \frac{\partial \omega_2}{\partial z} \tag{17}$$

According to Eqs. (16) and (17), the value of lattice curvature k_{21} and k_{23} can be determined by numerical differentiation of the crystal lattice rotation angles in the global coordinate system. In this simulation, k_{21} is the domain lattice curvature as the indentation direction parallels with the $z(x_3)$ axis.

The information of global coordinate systems of each node in our model was extracted before and after deformation to calculate the lattice rotation angles. Then, the values of lattice curvature k_{21} form Stage A to Stage C during indentation were converted to contour maps which are shown as in Fig. 14.
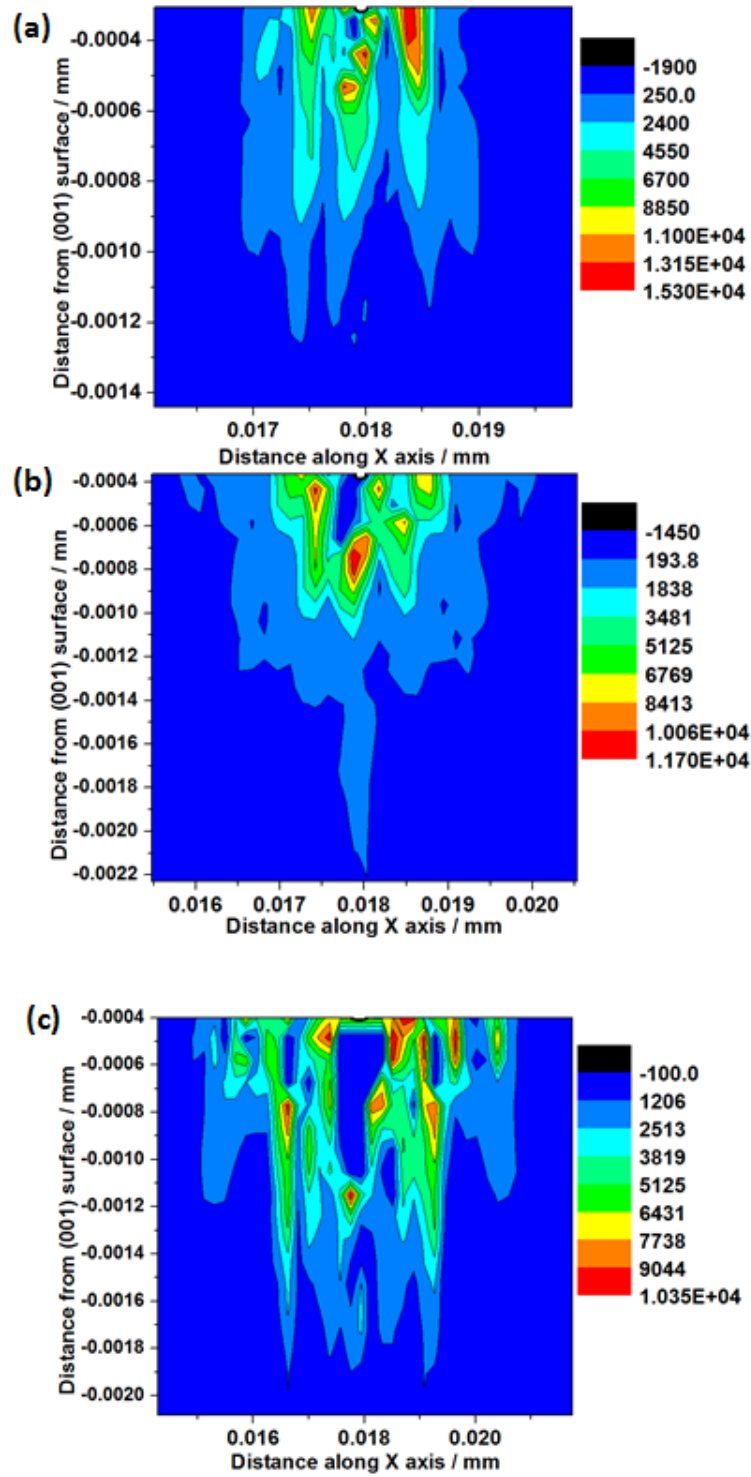
Fig. 14. The distribution of lattice curvature k_{21} at different stage during indentation: (a) stage A; (b) stage B; (c) stage C.

It is obvious the main lattice curvature k_{21} decreases with the increasing of the indentation depth from Stage A to Stage C, and the difference between Stage A and Stage B is much significant than that between Stage B and Stage C.

4. Conclusions:

1. A crystal plasticity finite element method (CPFEM) model has been developed to investigate the indentation size effect of aluminium single crystal during nano-indentation. The simulated results have been validated by comparison with experimental observations.

2. The load-displacement curve has been divided into two separate parts and fitted by two power relationships. It has been found that hardness significantly decreases with the indentation depth, while it remains nearly constant after the indentation depth exceeds a certain value.

3. The distribution of Mises stress and critical resolved shear stress has been investigated during three different stages of the indentation process. It has been found both the maximum Mises stress and critical resolved shear stress are located right under the indenter at Stage A, and then they start to split at Stage B. Eventually, the maximum Mises stress and critical resolved shear stress move to the side of the indenter.

4. The lattice curvature has been studied and simulated during three different stages of indentation process. It has been found the main lattice curvature k_{21} decreases with the indentation depth from Stage A to Stage C, and the difference between Stage A and Stage B is much significant than that between Stage B and Stage C.

References:

Arsenlis, A., Parks, D.M., 1999. Crystallographic aspects of geometrically-necessary and statistically-stored dislocation density. Acta Materialia 47, 1597-1611.

Asaro, R.J., 1983. Crystal Plasticity. J Appl Mech-T Asme 50, 921-934.

Bassani, J.L., Wu, T.Y., 1991. Latent Hardening in Single-Crystals .2. Analytical Characterization and Predictions. P Roy Soc Lond a Mat 435, 21-41.

Budiman, A.S., Han, S.M., Greer, J.R., Tamura, N., Patel, J.R., Nix, W.D., 2008. A search for evidence of strain gradient hardening in Au submicron pillars under uniaxial compression using synchrotron X-ray micro diffraction. Acta Materialia 56, 602-608.

Budiman, A.S., Nix, W.D., Tamura, N., Valek, B.C., Gadre, K., Maiz, J., Spolenak, R., Patel, J.R., 2006. Crystal plasticity in Cu damascene interconnect lines undergoing electromigration as revealed by synchrotron x-ray microdiffraction. Appl Phys Lett 88.

Ebisu, T., Horibe, S., 2010. Analysis of the indentation size effect in brittle materials from nanoindentation load-displacement curve. J Eur Ceram Soc 30, 2419-2426.

Feng, G., Budiman, A.S., Nix, W.D., Tamura, N., Patel, J.R., 2008. Indentation size effects in single crystal copper as revealed by synchrotron x-ray microdiffraction. J Appl Phys 104.

Fischer-Cripps, A.C., 2006. Critical review of analysis and interpretation of nanoindentation test data. Surface and Coatings Technology 200, 4153-4165.

Fischer-Cripps, A.C., 2009. The IBIS Handbook of Nanoindentation. Fischer-Cripps Laboratories Pty Ltd.

Fleck, N.A., Hutchinson, J.W., 1993. A Phenomenological Theory for Strain Gradient Effects in Plasticity. J Mech Phys Solids 41, 1825-1857.

Fleck, N.A., Hutchinson, J.W., 1997. Strain gradient plasticity. Adv Appl Mech 33, 295-361.

Fleck, N.A., Muller, G.M., Ashby, M.F., Hutchinson, J.W., 1994. Strain Gradient Plasticity - Theory and Experiment. Acta Metall Mater 42, 475-487.

Franciosi, P., Berveiller, M., Zaoui, A., 1980. Latent Hardening in Copper and Aluminum Single-Crystals. Acta Metall Mater 28, 273-283.

Gane, N., Cox, J.M., 1970. Micro-Hardness of Metals at Very Low Loads. Philos Mag 22, 881-&.

Gao, H., Huang, Y., Nix, W.D., 1999a. Modeling plasticity at the micrometer scale. Naturwissenschaften 86, 507-515.

Gao, H., Huang, Y., Nix, W.D., Hutchinson, J.W., 1999b. Mechanism-based strain gradient plasticity - I. Theory. Journal of the Mechanics and Physics of Solids 47, 1239-1263.

Gong, J., Wu, J., Guan, Z., 1999. Examination of the indentation size effect in low-load vickers hardness testing of ceramics. J Eur Ceram Soc 19, 2625-2631.

Gong, J.H., Zhao, Z., Guan, Z.D., Miao, H.Z., 2000. Load-dependence of Knoop hardness of Al2O3-TiC composites. J Eur Ceram Soc 20, 1895-1900.

Hill, R., 1966. Generalized constitutive relations for incremental deformation of metal crystals by multislip. Journal of the Mechanics and Physics of Solids 14, 95-102.

Huang, Y., Gao, H., Nix, W.D., Hutchinson, J.W., 2000. Mechanism-based strain gradient plasticity - II. Analysis. Journal of the Mechanics and Physics of Solids 48, 99-128.

Huang, Y.G., 1991. A user-material subroutine incorporating single crystal plasticity in the ABAQUS finite element program. Harvard University.

Huynh, N.N., Lu, C., Si, L., Tieu, K., 2008. A study of microstructural evolution around crack tip using crystal plasticity finite-element method. Proceedings of the Institution of Mechanical Engineers Part J-Journal of Engineering Tribology 222, 183-192.

Kiener, D., Durst, K., Rester, M., Minor, A.M., 2009. Revealing deformation mechanisms with nanoindentation. Jom-Us 61, 14-23.

Kiener, D., Pippan, R., Motz, C., Kreuzer, H., 2006. Microstructural evolution of the deformed volume beneath microindents in tungsten and copper. Acta Materialia 54, 2801-2811.

Kolemen, U., 2006. Analysis of ISE in microhardness measurements of bulk MgB2 superconductors using different models. J Alloy Compd 425, 429-435.

Kysar, J.W., Gan, Y.X., Morse, T.L., Chen, X., Jones, M.E., 2007. High strain gradient plasticity associated with wedge indentation into face-centered cubic single crystals: Geometrically necessary dislocation densities. Journal of the Mechanics and Physics of Solids 55, 1554-1573.

Li, H., Bradt, R.C., 1993. The Microhardness Indentation Load Size Effect in Rutile and Cassiterite Single-Crystals. Journal of Materials Science 28, 917-926.

Li, H., Ghosh, A., Han, Y.H., Bradt, R.C., 1993. The Frictional Component of the Indentation Size Effect in Low Load Microhardness Testing. J Mater Res 8, 1028-1032.

Liu, M., Lu, C., Tieu, K., Yu, H., 2014. Numerical comparison between Berkovich and conical nano-indentations: Mechanical behaviour and micro-texture evolution. Materials Science and Engineering: A 619, 57-65.

Liu, Y., Varghese, S., Ma, J., Yoshino, M., Lu, H., Komanduri, R., 2008. Orientation effects in nanoindentation of single crystal copper. International Journal of Plasticity 24, 1990-2015.

Liu, Y., Wang, B., Yoshino, M., Roy, S., Lu, H., Komanduri, R., 2005. Combined numerical simulation and nanoindentation for determining mechanical properties of single crystal copper at mesoscale. Journal of the Mechanics and Physics of Solids 53, 2718-2741.

Lu, C., Deng, G.Y., Tieu, A.K., Su, L.H., Zhu, H.T., Liu, X.H., 2011. Crystal plasticity modeling of texture evolution and heterogeneity in equal channel angular pressing of aluminum single crystal. Acta Materialia 59, 3581-3592.

Ma, Clark, 1995. Size dependent hardness in silver single crystals. J. Mater. Res., 10, 853-863.

McElhaney, K.W., Vlassak, J.J., Nix, W.D., 1998. Determination of indenter tip geometry and indentation contact area for depth-sensing indentation experiments. J Mater Res 13, 1300-1306.

Nix, W.D., Gao, H.J., 1998. Indentation size effects in crystalline materials: A law for strain gradient plasticity. J Mech Phys Solids 46, 411-425.

Nye, J.F., 1953. Some geometrical relations in dislocated crystals. Acta Metall Mater 1, 153-162.

Peng, Z., Gong, J., Miao, H., 2004. On the description of indentation size effect in hardness testing for ceramics: Analysis of the nanoindentation data. J Eur Ceram Soc 24, 2193-2201.

Ren, X.J., Hooper, R.M., Griffiths, C., Henshall, J.L., 2003. Indentation size effect in ceramics: Correlation with H/E. Journal of Materials Science Letters 22, 1105-1106.

Rester, M., Motz, C., Pippan, R., 2007. Microstructural investigation of the volume beneath nanoindentations in copper. Acta Materialia 55, 6427-6435.

Sakai, M., 1993. Energy principle of the indentation-induced inelastic surface deformation and hardness of brittle materials. Acta Metallurgica et Materialia 41, 1751-1758.

Samuels, L.E., 1986. Microindentation in Metals, ASTM STP, Philadelphia, pp. 5-25.

Sargent, P.M., 1986. Use of the Indentation Size Effect on Microhardness for Materials Characterization, ASTM STP, Philadelphia, pp. 160-174.

Si, L.Y., Lu, C., Huynh, N.N., Tieu, A.K., Liu, X.H., 2008. Simulation of rolling behaviour of cubic oriented al single crystal with crystal plasticity FEM. Journal of Materials Processing Technology 201, 79-84.

Stelmashenko, N.A., Walls, M.G., Brown, L.M., Milman, Y.V., 1993. Microindentations on W and Mo Oriented Single-Crystals - an Stm Study. Acta Metallurgica et Materialia 41, 2855-2865.

Sun, S., Adams, B.L., King, W.E., 2000. Observations of lattice curvature near the interface of a deformed aluminium bicrystal. Philos Mag A 80, 9-25.

Swadener, J.G., George, E.P., Pharr, G.M., 2002. The correlation of the indentation size effect measured with indenters of various shapes. J Mech Phys Solids 50, 681-694.

Voyiadjis, G.Z., Peters, R., 2010. Size effects in nanoindentation: an experimental and analytical study. Acta Mech 211, 131-153.

Wert, J.A., Liu, Q., Hansen, N., 1997. Dislocation boundary formation in a cold-rolled cube-oriented Al single crystal. Acta Mater 45, 2565-2576.

Zaafarani, N., Raabe, D., Singh, R.N., Roters, F., Zaefferer, S., 2006. Three-dimensional investigation of the texture and microstructure below a nanoindent in a Cu single crystal using 3D EBSD and crystal plasticity finite element simulations. Acta Materialia 54, 1863-1876